entropy

IMPACT FACTOR 2.738

Indexed in: PubMed

Article

Dynamical Quantum Phase Transitions of the Schwinger Model: Real-Time Dynamics on IBM Quantum

Domenico Pomarico, Leonardo Cosmai, Paolo Facchi, Cosmo Lupo, Saverio Pascazio and Francesco V. Pepe

Special Issue

Current Trends in Quantum Phase Transitions II

Edited by

Dr. Miguel A. Bastarrachea-Magnani

MDPI

https://doi.org/10.3390/e25040608

entropy

MDPI

Article

Dynamical Quantum Phase Transitions of the Schwinger Model: Real-Time Dynamics on IBM Quantum

Domenico Pomarico [1,2,*], Leonardo Cosmai [2], Paolo Facchi [1,2], Cosmo Lupo [2,3], Saverio Pascazio [1,2] and Francesco V. Pepe [1,2]

[1] Dipartimento di Fisica, Università di Bari, I-70126 Bari, Italy; paolo.facchi@ba.infn.it (P.F.); saverio.pascazio@ba.infn.it (S.P.); francesco.pepe@ba.infn.it (F.V.P.)
[2] Istituto Nazionale di Fisica Nucleare, Sezione di Bari, I-70126 Bari, Italy; leonardo.cosmai@ba.infn.it (L.C.); cosmo.lupo@poliba.it (C.L.)
[3] Dipartimento di Fisica, Politecnico di Bari, I-70126 Bari, Italy
* Correspondence: domenico.pomarico@ba.infn.it

Abstract: Simulating the real-time dynamics of gauge theories represents a paradigmatic use case to test the hardware capabilities of a quantum computer, since it can involve non-trivial input states' preparation, discretized time evolution, long-distance entanglement, and measurement in a noisy environment. We implemented an algorithm to simulate the real-time dynamics of a few-qubit system that approximates the Schwinger model in the framework of lattice gauge theories, with specific attention to the occurrence of a dynamical quantum phase transition. Limitations in the simulation capabilities on IBM Quantum were imposed by noise affecting the application of single-qubit and two-qubit gates, which combine in the decomposition of Trotter evolution. The experimental results collected in quantum algorithm runs on IBM Quantum were compared with noise models to characterize the performance in the absence of error mitigation.

Keywords: noisy intermediate-scale quantum devices; quantum electrodynamics; dynamical quantum phase transition

check for updates

Citation: Pomarico, D.; Cosmai, L.; Facchi, P.; Lupo, C.; Pascazio, S.; Pepe, F.V. Dynamical Quantum Phase Transitions of the Schwinger Model: Real-Time Dynamics on IBM Quantum. *Entropy* **2023**, *25*, 608. https://doi.org/10.3390/e25040608

Academic Editor: Miguel A. Bastarrachea-Magnani

Received: 29 December 2022
Revised: 17 March 2023
Accepted: 29 March 2023
Published: 3 April 2023

Copyright: © 2023 by the authors. Licensee MDPI, Basel, Switzerland. This article is an open access article distributed under the terms and conditions of the Creative Commons Attribution (CC BY) license (https://creativecommons.org/licenses/by/4.0/).

1. Introduction

The availability of noisy intermediate-scale quantum (NISQ) devices in cloud access platforms is a fundamental step towards the quantum computing era. Nonetheless, the limited number of available qubits and the absence of controllable error probabilities prevents these systems from actually outperforming current classical computing capabilities. Multiple hardware setups have been engineered for quantum computing purposes, with different advantages regarding gates' fidelity and experimental realization. Examples of NISQ devices are represented by circuits with superconducting transmon qubits [1–3], ion traps or optical lattices hosting Rydberg atoms [4–8], and qubits encoded in photonic modes of optical setups [9,10], this list being far from exhaustive.

In this framework, high-energy physics represents an interesting testbed for quantum devices. On the one hand, quantum computation can be applied "downstream", to optimize data analysis and event reconstruction from experiments [11–15]. On the other hand, the "upstream" investigation of gauge theories, especially in their lattice formulation [16–20], can benefit from the possibility of performing quantum simulations of regimes not achievable with perturbative techniques. Long-standing questions related to low-energy processes in quantum chromodynamics (QCD) are still far from the current capabilities of Monte Carlo techniques, due to the sign problem in fermionic amplitudes [21–23]. To overcome some of these limitations, research at the interface of quantum information, condensed-matter, and high-energy physics is targeting the adoption of new theoretical and computational tools. The state-of-the-art in the field is represented by tensor network methods, able to reduce the exponential complexity to a polynomial one for states characterized by short-range

entanglement [24–30]. These methods are suitable candidates to obtain a breakthrough in non-perturbative regimes: some preliminary studies about quantum electrodynamics (QED) in one spatial dimension proved the ability of tensor networks in describing a wide phenomenology, such as vacuum phase transition, the string-breaking mechanism, and scattering processes [31–33]. On the other hand, highly entangled quantum systems must be studied by means of specifically designed setups, since their complexity cannot be managed with current classical computing capabilities.

A major role in making quantum computation and simulation effective to solve practical problems in NISQ devices is played by error correction and mitigation [34–36]. In the context of digital real-time evolution [37–42], such procedures should keep the quantum state of the system in the physical subspaces allowed by the gauge constraint. Unfortunately, these techniques are expected to limit the quantum advantage due to the required classical information processing. Nevertheless, current simulations on NISQ devices would benefit from the aforementioned techniques in the description of targeted physical phenomena. The hardest operation for any device is represented by a controlled gate, whose implementation varies in each platform, as with ion traps [4,41,42] or superconducting circuits [37–40]. These setups elaborate single-qubit states by means of laser pulses, tuned with the targeted transitions. Instead, entangling gates are specifically engineered by exploiting the properties of the hardware, thus leading to crucially different fidelities and times required for the physical implementation. Alternatively, analog simulations, e.g., in optical lattices, can adopt different strategies, such as a periodic drive to obtain energy terms endowed with the same symmetry characterizing lattice QED [43,44]. In this case, errors can induce gauge-invariance-breaking terms, which can lead to an emergent prethermal behavior [45–48].

This paper aimed at testing the superconducting qubit systems available in the IBM Quantum platform [1] in a simple lattice gauge theory application. We implemented digital evolutions generated by the QED Hamiltonian in $1+1$ dimensions, consisting of non-commuting local contributions [4,31–33,37,41,49–56] and displaying the occurrence of dynamical quantum phase transitions (DQPTs) [57–59] in specific cases of quantum quenches. A discretization of the electromagnetic field is required to implement gauge degrees of freedom in the quantum simulator: accomplishing such a task by replacing the continuous $\mathrm{U}(1)$ gauge group with one of the cyclic groups $\mathbb{Z}_n$ guarantees a unitary implementation of the gauge connections [49]; another possible choice is represented by the family of quantum link models [60]. In order to assign each link of the lattice to a single qubit, we chose a $\mathbb{Z}_2$ discretization, which ensures a minimal circuit depth [52], thus reducing error sources. The study of real-time dynamics involves three crucial stages: the preparation of initial states, the evolution, and the final measurements. Gate errors affecting a digital simulation accumulate in a more or less coherent manner, which is affected by more variables and more error sources than the stand-alone characterization of gates. Time evolution is partitioned into steps to monitor the measurements statistics' variation without the inclusion of error correction and mitigation. The ground state preparation required by the chosen quench protocol was specifically designed in order to minimize errors and characterize the first stage's output statistics. Then, we characterized the effectiveness of time evolution, choosing to analyze the system in proximity of a DQPT, where the dynamics is particularly sensitive to noise [51], thus framing the simulation in most unsafe conditions. A concluding estimation of the amount of error probability reduction required for a partial observation of the targeted DQPT was made by analyzing the statistics of the collected results.

The paper is structured as follows. In Section 2, we introduce the lattice Schwinger model and the Jordan–Wigner transformation that maps it into a qubit system and describe the quench protocol and the DQPTs expected in the model. In Section 3, we describe the experimental scheme composed of ground state preparation and the subsequent Trotter evolution. The collected results are compared with the simulated evolution affected by the error probabilities of noisy gates. In Section 4, we discuss our outcomes in light of the existing literature and present a possible outlook for our research.

2. The Lattice Schwinger Model

QED in $1+1$ dimensions, also known as the Schwinger model, is a U(1) gauge theory describing the interaction of the electromagnetic field, consisting of only an electric component, and a fermionic particle with mass m and charge g. The model can be discretized on a one-dimensional lattice with spacing a, by associating with each lattice site x an anticommuting field ψ_x, which represents a spinless fermion, while links between each pair of neighboring sites host the gauge degrees of freedom, described by the electric field $E_{x,x+1}$ and the vector potential $A_{x,x+1}$. The latter determines the gauge connection $U_{x,x+1} = e^{iaA_{x,x+1}}$, characterized by the generalized canonical commutation relation $[E_{x',x'+1}, U_{x,x+1}] = \delta_{x,x'} U_{x,x+1}$. The lattice model Hamiltonian for a finite lattice with N sites reads [4,31–33,49]

$$H = -\frac{i}{2a}\sum_{x=0}^{N-1}\left(\psi_x^\dagger U_{x,x+1}\psi_{x+1} - \text{H.c.}\right) + m\sum_{x=0}^{N-1}(-1)^x\psi_x^\dagger\psi_x + \frac{g^2a}{2}\sum_{x=0}^{N-1}E_{x,x+1}^2, \tag{1}$$

where periodic boundary conditions [50,51] require the identification $N \equiv 0$. The model involves staggered (Kogut–Susskind) fermions [61], described by single-component spinors ψ_x, with negative-mass components encoded in odd-x sites. The physical subspace $\mathscr{H}_G$ is spanned by states $|\phi\rangle$ satisfying the Gauss law constraint $G_x|\phi\rangle = 0$ at all sites x, where, for a $\mathbb{Z}_n$ gauge group,

$$G_x = \sqrt{\frac{n}{2\pi}}(E_{x,x+1} - E_{x-1,x}) - \psi_x^\dagger\psi_x - \frac{(-1)^x - 1}{2}. \tag{2}$$

The electric field was simulated in the following through a $\mathbb{Z}_n$ discretization of U(1) [31–33,49,52,53] with $n = 2$. Unlike in the quantum link models [50,51], where the electric field is replaced by a spin operator, the $\mathbb{Z}_n$ model is based on replacing gauge connections with permutation matrices [49]. In the case of $\mathbb{Z}_2$, the electric field in each link $(x, x+1)$ can have two eigenstates, which will be labeled as $\{|\ell = \frac{1}{2}\rangle_x, |\ell = -\frac{1}{2}\rangle_x\}$, with

$$E_{x,x+1}\left|\pm\frac{1}{2}\right\rangle_x = \pm\frac{\sqrt{\pi}}{2}\left|\pm\frac{1}{2}\right\rangle_x, \tag{3}$$

while the gauge connections act as [31–33]

$$U_{x,x+1}\left|\pm\frac{1}{2}\right\rangle_x = \left|\mp\frac{1}{2}\right\rangle_x. \tag{4}$$

An immediate implication of the $\mathbb{Z}_2$ model is the irrelevance in the Hamiltonian (1) of the electric field energy, which becomes a constant.

The simplest nontrivial periodic lattice is composed by $N = 2$ sites: the states spanning the physical subspace $\mathscr{H}_G$ of the $\mathbb{Z}_2$ model in this simple case are shown in Figure 1. The states in Panels (a) and (d) represent two "Dirac vacua", with a filled negative-mass and an empty positive-mass site. In these states, the total electric field is constant and nonvanishing. These observations motivated the notation $|vac\rangle_\pm$ for these two states, where the index is related to the sign of the background electric field. Particle hopping leads to the remaining "mesonic" basis states $|e^+e^-\rangle_L$ and $|e^+e^-\rangle_R$, represented in Panels (b) and (c), respectively, where the index refers to the counterclockwise (L) or clockwise (R) hopping of the fermion from the negative- to the positive-mass site.

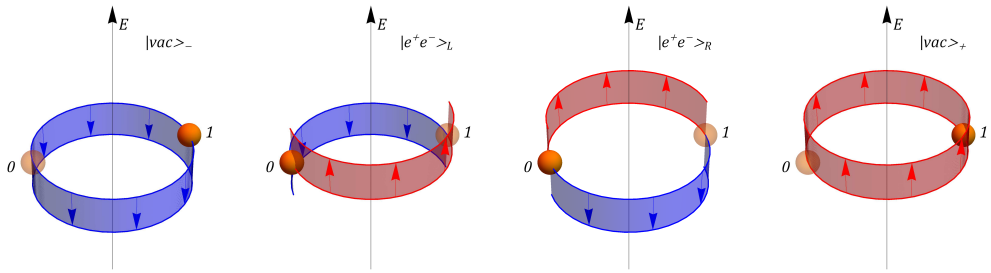

(**a**) (**b**) (**c**) (**d**)

Figure 1. Representation of the physical subspace basis states in a $\mathbb{Z}_n$ gauge model, implemented on a two-site lattice. In all panels, full (transparent) spheres represent occupied (empty) matter sites, while red (blue) edges correspond to a positive (negative) electric field on a link. Panels (**a**,**d**) represent "Dirac vacua", characterized by an occupied negative-mass fermion site, an empty positive-mass fermion site, and a constant background electric field. Panels (**b**,**c**) represent "meson" states, with an occupied positive-mass fermion site, an empty negative-mass fermion site (corresponding to an antiparticle), and a staggered electric field.

The Jordan–Wigner transformation maps the spinor field into a spin system [4,52], which corresponds to our qubit register, as

$$\psi_x = \prod_{\ell<x}(\mathrm{i}Z_\ell)\frac{X_x+\mathrm{i}Y_x}{2}, \qquad \psi_x^\dagger = \prod_{\ell<x}(-\mathrm{i}Z_\ell)\frac{X_x-\mathrm{i}Y_x}{2}, \tag{5}$$

where X, Y, and Z are Pauli matrices, $\sigma^\pm = \frac{X\pm\mathrm{i}Y}{2}$, and occupied sites correspond to qubit states $|\downarrow\rangle$. The Hamiltonian of the resulting spin system is

$$H = H_J + H_m = \frac{J}{2}\sum_{x=0}^{N-1}\left(\sigma_x^- U_{x,x+1}\sigma_{x+1}^+ + \mathrm{H.c.}\right) - \frac{m}{2}\sum_{x=0}^{N-1}(-1)^x Z_x = \sum_{x=0}^{N-1} h_x, \tag{6}$$

where the free parameter corresponds to a coupling constant $J = \frac{1}{a}$, once energy is scaled in units of mass m.

2.1. Dynamical Quantum Phase Transitions

We aimed at studying the non-equilibrium dynamics of the described lattice Schwinger model following a quantum quench [50,51,57]. Generally, in this protocol, one considers a family of Hamiltonians $H(\gamma)$ that depends on a tunable parameter and prepares an initial state coinciding with the ground state $|\psi_g\rangle$ of $H_0 = H(\gamma_0)$. At $t = 0$, the Hamiltonian suddenly switches to $H = H(\gamma_f)$, determining the evolution $|\psi(t)\rangle = \mathrm{e}^{-\mathrm{i}tH}|\psi_g\rangle$, characterized by the survival (or Loschmidt) amplitude:

$$\mathcal{G}(t) = \langle\psi_g|\psi(t)\rangle\,. \tag{7}$$

To identify a possible DQFT, we search for the zeros of the *Loschmidt echo*:

$$\mathcal{L}(t) = |\mathcal{G}(t)|^2 = \mathrm{e}^{-N\lambda(t)}, \tag{8}$$

which depends on the number N of degrees of freedom and on the rate function $\lambda(t)$, which becomes divergent in correspondence with the aforementioned zeros.

The targeted evolution generated by the Hamiltonian (6) is determined by a single free parameter, as the Loschmidt amplitude phase $\varphi(J,t) = \arg\mathcal{G}(t)$ is undefined in

correspondence with the critical points. Nonetheless, in their neighborhood, φ is expected to be smooth up to a discontinuity line of 2π starting from the criticality. This characterization corresponds to a vortex, with a winding number:

$$\nu = \frac{1}{2\pi} \oint_{\mathcal{C}} \mathrm{d}\boldsymbol{s} \cdot \boldsymbol{\nabla} \varphi, \tag{9}$$

where $\mathcal{C}$ is a loop in the (J, t) plane [50].

The adopted protocol quenches the Kogut–Susskind staggered fermions at $t = 0$ by inverting the mass sign: $H(m, J) \longrightarrow H(-m, J)$. The quenched Hamiltonian can be decomposed into parity sectors, as described in Appendix A:

$$H(-m, J) = H^{(-)} \oplus H^{(+)}. \tag{10}$$

In the even sector, the evolution is generated by

$$H^{(+)} = \begin{pmatrix} -\frac{J^2-m^2}{\sqrt{m^2+J^2}} & \frac{2Jm}{\sqrt{m^2+J^2}} \\ \frac{2Jm}{\sqrt{m^2+J^2}} & \frac{J^2-m^2}{\sqrt{m^2+J^2}} \end{pmatrix}, \tag{11}$$

in the subspace spanned by the basis $\{|\psi_g\rangle, |\psi_{\bar{g}}\rangle\}$, made of the even eigenstates of the initial Hamiltonian $H_0 = H(m, J)$, which are associated with the lowest and highest eigenvalue $E_g = -\sqrt{m^2 + J^2}$ and $E_{\bar{g}} = +\sqrt{m^2 + J^2}$, respectively. The odd parity sector involves the eigenstates $|\psi_e\rangle$ and $|\psi_{\bar{e}}\rangle$ of $H(m, J)$, which are independent of J and characterized by the eigenvalues $\pm m$; these two states are still eigenstates of the quenched Hamiltonian $H(-m, J)$, which only inverts their eigenvalues.

The Loschmidt amplitude for the initial ground state:

$$|\psi_g\rangle = a_g(|vac\rangle_+ + |vac\rangle_-) + b_g(|e^+e^-\rangle_L + |e^+e^-\rangle_R), \tag{12}$$

derived in Appendix A, reads

$$\mathcal{G}(t) = (2a_g^2 - 2b_g^2)^2 \mathrm{e}^{-\mathrm{i}E_g t}\left(1 + \frac{J^2}{m^2}\mathrm{e}^{-\mathrm{i}(E_{\bar{g}} - E_g)t}\right), \tag{13}$$

with

$$a_g = \frac{1}{\sqrt{2\left(1 + p_g^2\right)}}, \quad b_g = \frac{p_g}{\sqrt{2\left(1 + p_g^2\right)}}, \quad \text{with } p_g = \frac{m}{J} - \sqrt{\frac{m^2}{J^2} + 1}. \tag{14}$$

DQPTs are observed for $J = m$ at times

$$t_j = \frac{(2j+1)\pi}{2E_{\bar{g}}} = \frac{(2j+1)\pi}{2\sqrt{2}\, m}, \tag{15}$$

yielding the Rabi oscillations between $|\psi_g\rangle$ and $|\psi_{\bar{g}}\rangle$ expected from Equation (11), as shown in Figure 2. The behavior of the phase, reported in Figure 2b, features vortices corresponding to Loschmidt echo nodes, while the remaining discontinuities in survival maximum values compensate each other.

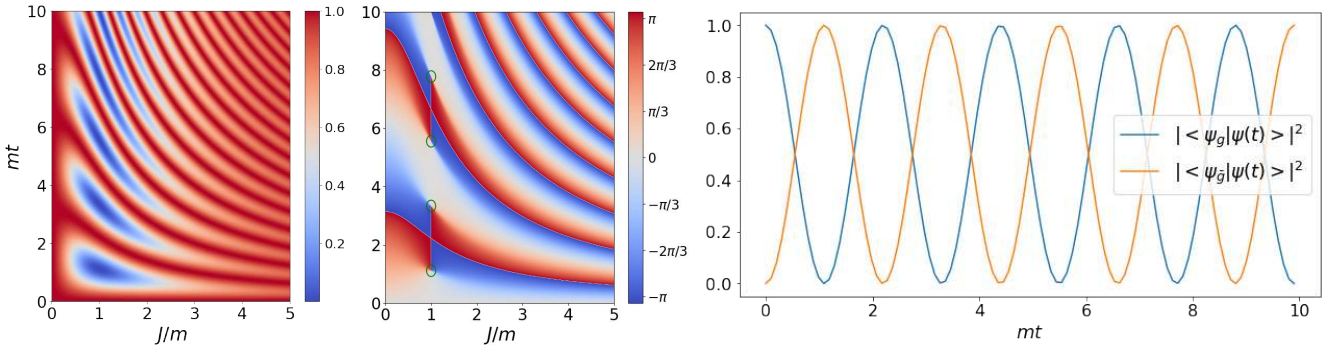

Figure 2. Panel (**a**) shows the Loschmidt echo $\mathcal{L}(t) = |\langle\psi_g|\psi(t)\rangle|^2$ with the variation of the free parameter J, while the phase of the Loschmidt amplitude is represented in Panel (**b**); here, the green paths around the DQPT points are characterized by a nonvanishing winding number. The Trotter evolution discussed in Section 2.4 of Rabi states with step $\Delta t = 0.1$, corresponding to $J/m = 1$ and without noise, is shown in Panel (**c**).

2.2. Ground State Preparation

The protocol presented in Section 2.1 requires the preparation of the input state $|\psi_g\rangle$, namely the ground state of $H(m, J)$. Based on reasons clarified in Section 2.4, the degrees of freedom of the lattice are assigned to the four qubits of the `ibmq_manila` circuit $|q_0q_1q_2q_3\rangle$:

- q_0 and q_3 host the "electric field" states of the $\mathbb{Z}_2$ links;
- The staggered spinless fermions are encoded in q_1 and q_2.

The four physical states refer to the following computational basis states: $|vac\rangle_- = |1011\rangle$, $|e^+e^-\rangle_L = |0101\rangle$, $|e^+e^-\rangle_R = |1100\rangle$, and $|vac\rangle_+ = |0010\rangle$, expressed according to the IBM `qiskit` notation $|\uparrow\rangle = |0\rangle$ and $|\downarrow\rangle = |1\rangle$ for matter sites and $|\frac{1}{2}\rangle = |0\rangle$ and $|-\frac{1}{2}\rangle = |1\rangle$ for links. Since each state can be unambiguously identified by the first two qubits $|q_0q_1\rangle$, one can associate with the ground state $|\psi_g\rangle$ an auxiliary *product* state of two qubits:

$$|\psi'_g\rangle = a_g(|10\rangle + |00\rangle) + b_g(|01\rangle + |11\rangle) = \frac{1}{\sqrt{2}}(|0\rangle + |1\rangle) \otimes \sqrt{2}(a_g|0\rangle + b_g|1\rangle), \tag{16}$$

with the amplitudes corresponding, in the DQPT condition $J/m = 1$, to $a_g = 0.653$ and $b_g = -0.271$.

The ground state for the complete four-qubit system is obtained by acting with $CNOT$ two-qubit gates:

$$CNOT_{ij}|q_iq_j\rangle = |q_i, q_i \oplus q_j\rangle, \tag{17}$$

which increase the amount of entanglement in the system. For this reason, containing the error probability entailed by these gates is essential to guarantee an effective quantum computation, which cannot be efficiently simulated by classical computers. The circuit chosen for the ground state preparation reads

$$|\psi_g\rangle = CNOT_{32}\, CNOT_{03}\, CNOT_{13}\, CNOT_{02}\, X_2|\psi'_g\rangle \otimes |00\rangle, \tag{18}$$

and is pictorially represented in Figure 3.

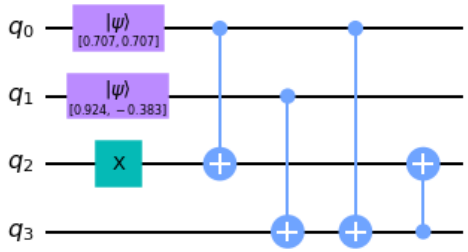

Figure 3. Circuit for the ground state preparation of $H(m, J)$ corresponding to the dynamical quantum phase transition value $J/m = 1$. Matter sites correspond to q_1 and q_2, while $\mathbb{Z}_2$ links are encoded in q_0 and q_3.

2.3. Noise Models

The simulation of the circuits included an error probability entailed by each gate application, generally described by the bit flip and phase flip error channel $\rho \mapsto \mathcal{D}[\rho] = \sum_{i=0}^{3} K_i \rho K_i^\dagger$, with

$$K_0 = \sqrt{1 - p_x - p_y - p_z}\, \mathbb{1}, \quad K_1 = \sqrt{p_x}\, X, \quad K_2 = \sqrt{p_y}\, Y, \quad K_3 = \sqrt{p_z}\, Z. \tag{19}$$

Such quantum channels, explicitly analyzed in Appendix B, are associated with every single-qubit gate employed both in the state preparation and in its time evolution, while for the two-qubit gates, the independent error probabilities (p_x, p_y, p_z) can be varied in Equation (19) to define

$$\rho \mapsto \widetilde{\mathcal{D}}[\rho] = \sum_{i,j=0}^{3} \widetilde{K}_{ij} \rho \widetilde{K}_{ij}^\dagger \qquad \text{with} \qquad \widetilde{K}_{ij} = K_i \otimes K_j \tag{20}$$

for a two-qubit density matrix ρ. Each circuit includes also reset and measurement gates, which are affected in the simulations only by bit flips [62,63], implemented by a single noise contribution K_1, thus corresponding to $p_z = p_y = 0$.

The comparison of the simulations with the outputs of IBM Quantum was evaluated in terms of the trace distance:

$$T(\rho_{\text{ibmq}}, \rho_{\text{sim}}) = \frac{1}{2} ||\rho_{\text{ibmq}} - \rho_{\text{sim}}||_1 = \frac{1}{2} \text{Tr}\left[\sqrt{(\rho_{\text{ibmq}} - \rho_{\text{sim}})^\dagger (\rho_{\text{ibmq}} - \rho_{\text{sim}})}\right], \tag{21}$$

which quantifies the similarity between the output state of simulated state ρ_{sim} and the actual output of the IBM hardware ρ_{ibmq}.

2.4. Trotter Evolution

The evolution determined by the Hamiltonian (6), composed of non-commuting local terms h_x, can be approximated by a Trotter decomposition basis on local unitary operators:

$$e^{-iHt} = e^{-i\sum_x h_x t} = \left(e^{-ih_{N-1}\Delta t} e^{-ih_{N-2}\Delta t} \dots e^{-ih_0 \Delta t}\right)^{\frac{t}{\Delta t}} + \mathcal{O}(\Delta t). \tag{22}$$

The improved approximation that would in principle be provided by the Suzuki–Trotter formula [52] is not well suited in this framework, because it would require a larger number of gates for circuit implementation.

A decomposition of each term in Equation (22) according to the available set of gates was formulated in [52]. Here, we present its specific application to the $\mathbb{Z}_2$ gauge

group [31,49], where $U_{x,x+1} = U^{\dagger}_{x,x+1} = X_{x,x+1}$. The fermionic hopping contribution can be equivalently expressed as

$$H_J = \frac{J}{4} \sum_{x=0}^{N-1} [X_{x,x+1}(X_x X_{x+1} + Y_x Y_{x+1})] = \sum_{x=0}^{N-1} h_{J,x}. \tag{23}$$

The evolution related to the Trotter time steps generated by the three qubits' interaction in Equation (23) was implemented according to the Cartan decomposition [64–66]. Concerning the periodic lattice with $N = 2$ sites, we considered for clarity the hopping term $h_{J,0}$, acting on the subsystem $|q_0 q_1 q_2\rangle$:

$$e^{-ih_{J,0}\Delta t} = K^{\dagger} A K, \tag{24}$$

$$K = CNOT_{12}\ CNOT_{01}\ H_1\ H_0\ CNOT_{12}, \tag{25}$$

$$A = \mathbb{1} \otimes R_z(J\Delta t/2) \otimes R_z(-J\Delta t/2), \tag{26}$$

where H_i is the Hadamard gate acting on q_i and $R_z(\alpha) = e^{-iZ\alpha/2}$. The remaining term $h_{J,1}$ acts in an analogous way on the subsystem $|q_1 q_2 q_3\rangle$, as represented in Figure 4.

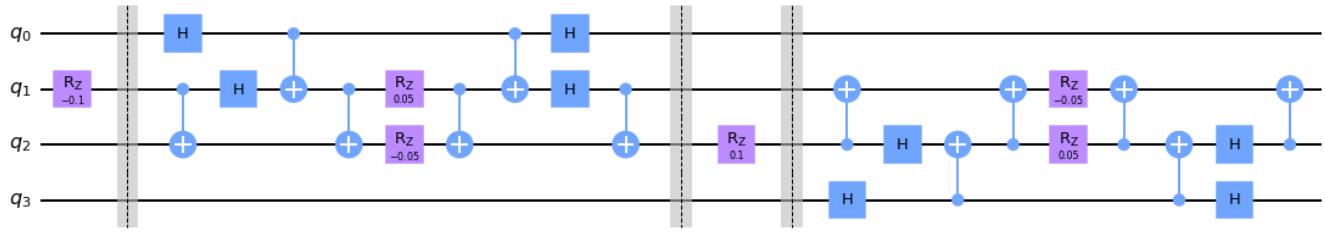

Figure 4. Trotter step as given in [52] for the $\mathbb{Z}_2$ gauge group discretization of lattice QED. Gauge degrees of freedom are encoded in qubits q_0 and q_3, while fermionic matter is described by qubits q_1 and q_2. The parameters used in R_z gates correspond to the choice $J = m = 1$ and $\Delta t = 0.1$.

The decomposition first rotates the product basis states:

$$|q_0\rangle \text{ —[H]—} \quad H_0\,|q_0\rangle = |\pm\rangle$$

$$\left.\begin{array}{l} |q_1\rangle \\ |q_2\rangle \end{array}\right\} \text{ [H] on } q_1 \text{, } \oplus \text{ on } q_2 \qquad (H_1 \otimes \mathbb{1})\ CNOT_{12}|q_1 q_2\rangle = \frac{|0\rangle + (-1)^{q_1}|1\rangle}{\sqrt{2}} \otimes |q_1 \oplus q_2\rangle = |Q_{q_1 q_2}\rangle$$

with $|\pm\rangle = |(-1)^{q_0}\rangle = \frac{1}{\sqrt{2}}(|0\rangle \pm |1\rangle)$ the X eigenstates. The action of Hadamard gate H_0 is required to entangle the state of the associated link with matter sites in the following steps:

$$\left.\begin{array}{l} |\pm\rangle \\ |Q_{q_1 q_2}\rangle \end{array}\right\} \text{ } \oplus \text{ on } q_1 \text{, } \oplus \text{ on } q_2$$

$$CNOT_{12}\ CNOT_{01}\ |\pm\rangle \otimes |Q_{q_1 q_2}\rangle = CNOT_{12}\ \frac{|00\rangle \pm |11\rangle + (-1)^{q_1}(|01\rangle \pm |10\rangle)}{2} \otimes |q_1 \oplus q_2\rangle$$

$$= \tfrac{1}{2}[(|00\rangle \pm (-1)^{q_1}|10\rangle) \otimes |q_1 \oplus q_2\rangle \pm (|11\rangle \pm (-1)^{q_1}|01\rangle) \otimes |\overline{q_1 \oplus q_2}\rangle] = |ZZ_{q_1 q_2}\rangle$$

where the bar stands for the logical NOT. A further elaboration of the above $|ZZ_{q_1 q_2}\rangle$ states expression simplifies the application of Cartan decomposition in the evolution with diagonal operators:

$$\begin{aligned} |ZZ_{q_1 q_2}(\Delta t)\rangle &= A|ZZ_{q_1 q_2}\rangle = \mathbb{1} \otimes R_z(J\Delta t/2) \otimes R_z(-J\Delta t/2)\left[|(-1)^{q_1}\pm\rangle \otimes \frac{1}{\sqrt{2}}(|0, q_1 \oplus q_2\rangle + (-1)^{q_1}|1, \overline{q_1 \oplus q_2}\rangle)\right] \\ &= |(-1)^{q_1}\pm\rangle \otimes \frac{1}{\sqrt{2}}\left(e^{-i\frac{J\Delta t}{4}(1-(-1)^{q_1 \oplus q_2})}|0, q_1 \oplus q_2\rangle + (-1)^{q_1} e^{i\frac{J\Delta t}{4}(1+(-1)^{\overline{q_1 \oplus q_2}})}|1, \overline{q_1 \oplus q_2}\rangle\right), \end{aligned} \tag{27}$$

such that states satisfying $q_1 \oplus q_2 = 1$ acquire a time-dependent phase, while there is no evolution outside the physical subspace $\mathscr{H}_G$ with $q_1 \oplus q_2 = 0$, as predicted by Equation (6).

Focusing on states with $q_1 \oplus q_2 = 1$, the next circuit steps related to $K^\dagger$ yield

$$\begin{aligned} |Q_{q_1 q_2}(\Delta t)\rangle &= CNOT_{01} CNOT_{12} |ZZ_{q_1 q_2}(\Delta t)\rangle \\ &= \frac{1}{2}\left(e^{-i\frac{J\Delta t}{2}}|00\rangle \pm (-1)^{q_1} e^{-i\frac{J\Delta t}{2}}|11\rangle + (-1)^{q_1} e^{i\frac{J\Delta t}{2}}|01\rangle \pm e^{i\frac{J\Delta t}{2}}|10\rangle\right) \otimes |1\rangle, \end{aligned} \tag{28}$$

followed by the last part of the decomposition:

$$CNOT_{12} H_1 H_0 |Q_{q_1 q_2}(\Delta t)\rangle = \begin{cases} \cos\frac{J\Delta t}{2}|001\rangle - i\sin\frac{J\Delta t}{2}|110\rangle, \text{ if } q_0 = 0, q_1 = 0, \\ \cos\frac{J\Delta t}{2}|101\rangle - i\sin\frac{J\Delta t}{2}|010\rangle, \text{ if } q_0 = 1, q_1 = 0, \\ \cos\frac{J\Delta t}{2}|010\rangle - i\sin\frac{J\Delta t}{2}|101\rangle, \text{ if } q_0 = 0, q_1 = 1, \\ \cos\frac{J\Delta t}{2}|110\rangle - i\sin\frac{J\Delta t}{2}|001\rangle, \text{ if } q_0 = 1, q_1 = 1, \end{cases} \tag{29}$$

as expected by the action of $e^{-iH_{J,0}\Delta t}$. Depending on states of the remaining link, encoded in $|q_3\rangle$, there are states not belonging to $\mathscr{H}_G$ that show a time evolution: they correspond to the ones shown in Figure 1 with a reversed matter site occupation. The remaining contributions in the Trotter expansion of Equation (22) are the diagonal mass terms $H_m = \sum_{x=0}^{N-1} h_{m,x}$ of Equation (6), expressed by

$$e^{-ih_{m,x}\Delta t} = R_z(-(-1)^x m\Delta t) = e^{i(-1)^x m Z_x \Delta t/2}, \tag{30}$$

as reported in Figure 4.

The topology of `ibmq_manila` in Figure 5a is well suited for the implementation of the Trotter evolution, since every CNOT involves nearest-neighbor qubits. In a noiseless scenario, the presented Trotter evolution would yield the Rabi oscillations in Figure 2c, corresponding to the analytical solution of the evolution by the quenched Hamiltonian.

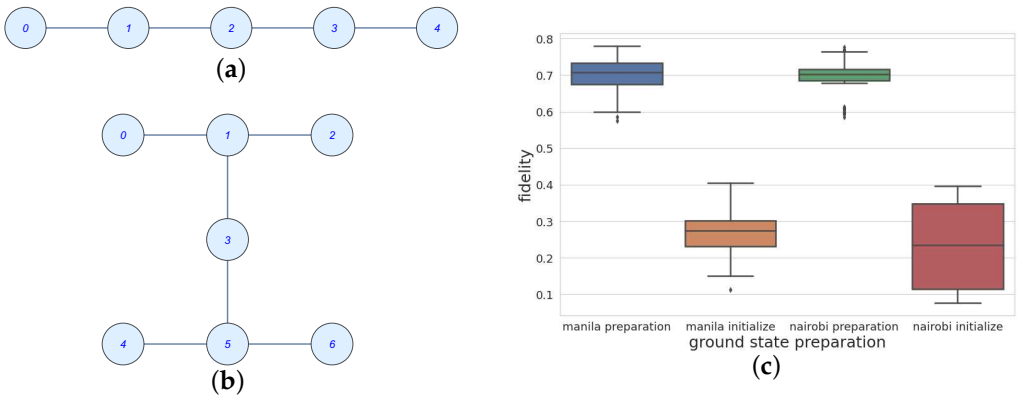

Figure 5. Topologies of the circuits `ibmq_manila`, in Panel (**a**), and `ibm_nairobi`, in Panel (**b**). The distributions of the ground state preparation fidelity obtained by applying the scheme proposed in Section 2.2 are compared with the output of the built-in command `QuantumCircuit.initialize` in the boxplot of Panel (**c**).

3. Simulations of Real-Time Dynamics

The experimental results presented in the following were collected in the IBM Quantum platform [1]. The circuit test was based on the simplest periodic lattice required for the implementation of the Schwinger model described in Section 2, composed of $N = 2$ sites for the matter field and an equal number of links endowed with the $\mathbb{Z}_2$ gauge group. This choice allows for the optimization of the number of gates involved in each Trotter time step, compared to higher-dimensional discretizations of the U(1) gauge group [52]. The simulations include a noise model referring to an error probability affecting each gate, but do not take into account effects related to coherence times, as discussed in Section 4.

The ground state preparation procedure presented in Section 2.2 performs better in terms of fidelity than the Python package `qiskit` built-in command `QuantumCircuit.initialize`, as shown in Figure 5. Errors due to the use of *CNOT* gates between non-neighboring qubits were investigated by implementing the same preparation in two different topologies, shown in Figure 5a,b: in `ibm_nairobi`, the qubits are encoded as follows (see the qubit labels in Panel (b)): $q_0 \rightarrow$ "2", $q_1 \rightarrow$ "0", $q_2 \rightarrow$ "3", $q_3 \rightarrow$ "1". Actually, Figure 3 shows the presence of three *CNOT* gates involving q_3, together with each one of the remaining qubits. For this reason, this is convenient to encoding it into the highest-degree node of Figure 5b, while the `ibm_nairobi` circuit is limited to the first four qubits. Despite their structural differences, the median values of the fidelities obtained with the `ibmq_manila` and `ibm_nairobi` topologies are essentially the same and are about 0.7, showing in both cases a much higher efficiency with respect to the implementation of `QuantumCircuit.initialize`. However, the collected statistics in Figure 5c, referring to 80 runs for each ground state preparation modality, shows that the interquartile range obtained with `ibm_nairobi` is smaller than the one provided by `ibmq_manila`. Moreover, fluctuations towards low values in the former case are much less relevant.

The readout of the output states is based on `state_tomography_circuits`, which exploits for our four-qubit circuit the Pauli basis, resulting in 3^4 circuits required by the related orthogonal measurements [67]. Simulated noise models include the effects of bit flips in the last measurement part of the circuit [62,63].

The ground state preparation was simulated by defining a noise model in `AerSimulator`. Three different models were compared with the `ibmq_manila` output through the trace distance defined in Equation (21) [68]. Each gate appearing in Figure 3 is affected by error probabilities expressed by the error channels (19)–(20). The simulations in Figure 6 use the following models of probability assignment:

(a) Single- and two-qubit gates share the same probability parameters (p_x, p_y, p_z), generally different along the three axes;
(b) Single-qubit gates have the same error probability along each noise direction $p_1 = p_x = p_y = p_z$; two-qubit gates have an analogous property, but are characterized by an independent probability p_2;
(c) Two parameters p_1 and p_2 quantify the error probability along both X and Z for single- and two-qubit gates, respectively, while errors along Y are neglected.

The simulations reported in Figure 6a were averaged over 20 realizations of the noise models, while those in Panels (b)–(c) were obtained from 50 realizations. Panel (a) shows a contour plot corresponding to each value of p_y, obtained by interpolating the trace distance evaluated over a grid consisting of 21×21 points with spacing 1×10^{-3} in the (p_x, p_z) plane. The considered output of `ibmq_manila` is a ground state averaged over 80 realizations. The mean value of the trace distance minimum in the variation of p_y is $10.81 \times 10^{-2} \pm 3.3 \times 10^{-3}$, attained at the averaged coordinates in the plane $(p_x, p_z) = ((10.7 \pm 1.1) \times 10^{-3}, (6.3 \pm 0.9) \times 10^{-3})$. These results are stable with respect to variations in p_y. Indeed, a Y error is provided by a sequence of simultaneous bit flips and phase flips, whose probability is much smaller than that of each single error. Panels (b)–(c) show the trace distance of the two noise models with independent parameters for single- and two-qubit gates with respect to the ground state ρ_{ibmq} experimentally prepared 80 times, with no error along Y in the case of Panel (c). The minimum values of the trace distance in the two cases can be considered equal within the statistical fluctuations. Moreover, the minima are found in correspondence with $(p_{1,xyz}, p_{2,xyz}) \simeq (5 \times 10^{-3}, 1 \times 10^{-2})$ in Panel (b) and $(p_{1,xz}, p_{2,xz}) \simeq (7.5 \times 10^{-3}, 1.5 \times 10^{-2})$ in Panel (c), highlighting a scale factor of $3/2$ due to the absence of the error along Y in the latter case. The minimum values of the trace distance, which equal 9.77×10^{-2} in Panel (b) and 11.16×10^{-2} in Panel (c), express the ability to distinguish the output ρ_{sim} from the experimental one ρ_{ibmq} approximately once out of ten times.

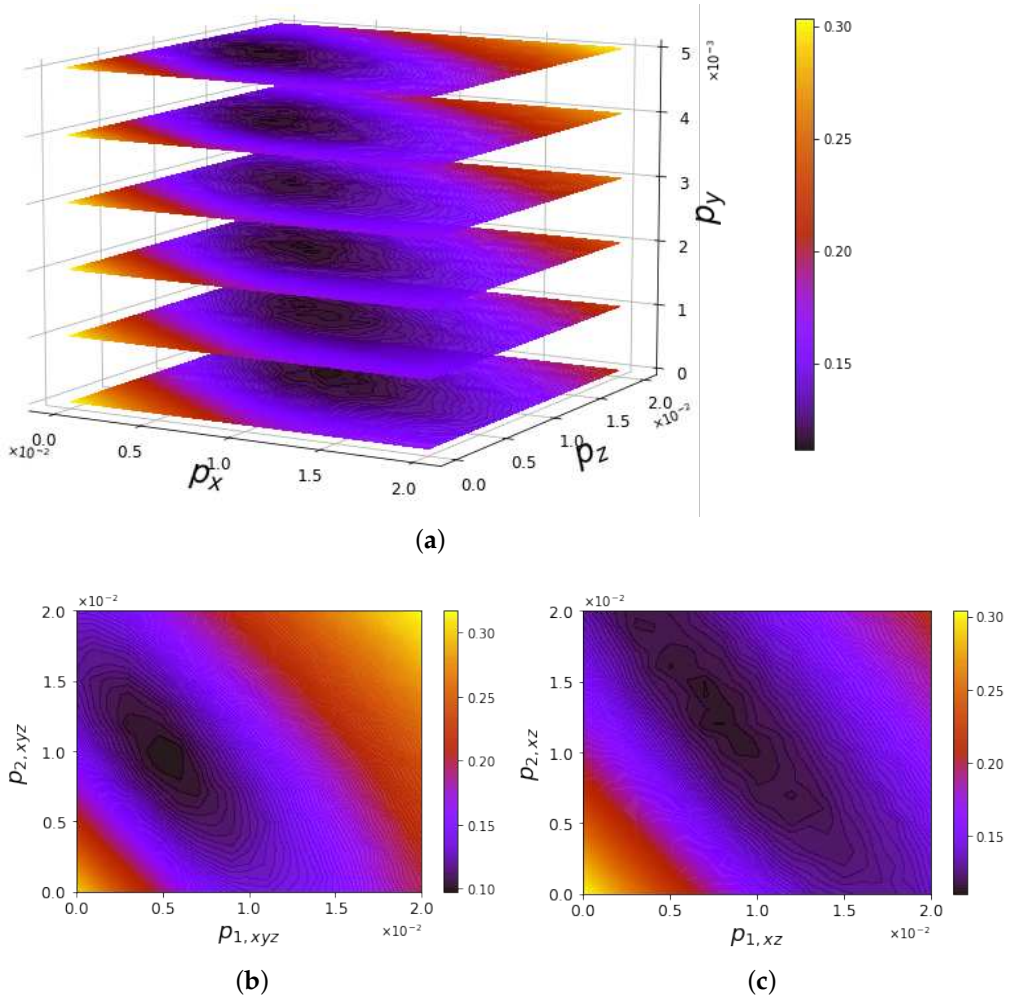

Figure 6. Trace distance $T(\rho_{\text{ibmq}}, \rho_{\text{sim}})$ of the simulated noise models affecting circuits' output with respect to the averaged ground state of `ibmq_manila` by varying the error probabilities. In Panel (**a**), contour plots in the plane (p_x, p_z) refer to different values of p_y. Panels (**b**,**c**) evaluate the variation in terms of single- and double-qubit gate error (p_1, p_2) with the inclusion or exclusion of Y errors, respectively.

The ground state in the input evolves according to the quench protocol presented in Section 2.1. Non-commuting local terms in the Hamiltonian, determined by the Jordan–Wigner transformation (6), are circumvented by means of the Trotter evolution described in Section 2.4, which was implemented using the `ibmq_manila` topology. The Loschmidt echo and the overlaps with the remaining physical states are shown in Figure 7, where the different curves were obtained by varying the time step length Δt and by averaging 10 experimental realizations of evolution for each case.

The high error probability translates into a fast convergence towards the maximally mixed state $\rho_\infty = (\dim \mathscr{H})^{-1}\mathbb{1}$. This trend shows a striking deviation for the probability $|\langle\psi_e|\psi(t)\rangle|^2$ during the first two time steps, probably driven by a coherent error accumulation. To focus on this behavior, as well as to limit the computational resources required in simulations, the trace distance is averaged over the first three time steps $t_i = (i-1)\Delta t$, using

$$\overline{T(\rho_{\text{ibmq}}, \rho_{\text{sim}})} = \frac{1}{3\Delta t}\sum_{i=1}^{3} T(\rho_{\text{ibmq}}(t_i), \rho_{\text{sim}}(t_i))\Delta t, \tag{31}$$

expressing the mean probability of distinguishing the evolution outputs of `ibmq_manila` from the simulated ones.

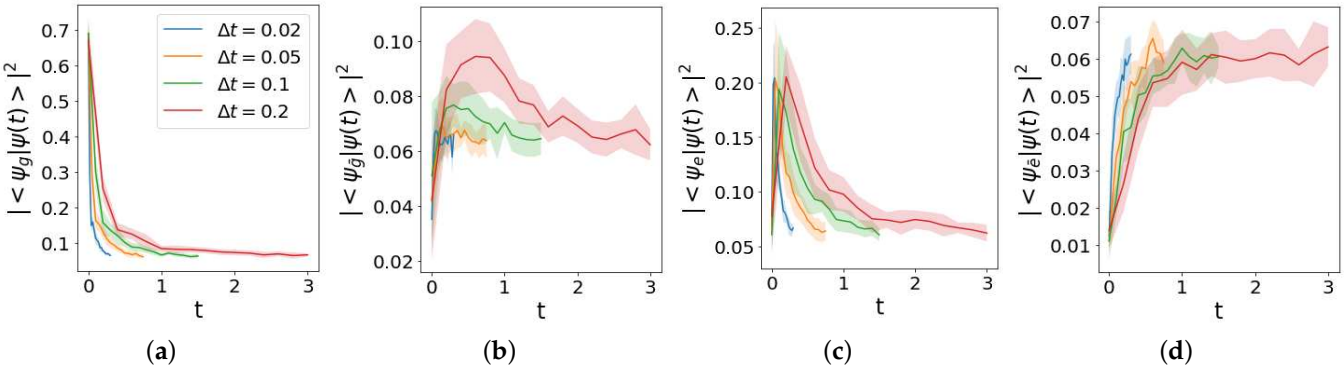

Figure 7. Trotter evolution of the initial state $|\psi_g\rangle$ for different time steps Δt, run in `ibmq_manila`. The average over 10 realizations corresponds to the solid line, while the shaded region represents the standard deviation. Loschmidt echo $|\langle\psi_g|\psi(t)\rangle|^2$ is shown in Panel (**a**), while probabilities of finding the evolved state in remaining physical states $|\psi_{\bar{g}}\rangle$, $|\psi_e\rangle$, $|\psi_{\bar{e}}\rangle$ are reported in Panel (**b**),(**c**),(**d**) respectively. Time is expressed in units of m^{-1} in all plots. The corresponding noiseless evolution is reported in Figure 2c.

The optimal error probabilities for the ground state preparation are identified in Figure 6c. Simulations of the evolution including noise models fix these parameters assigned to the gates in Figure 3. The Trotter evolution given in Figure 4 includes gates affected by error probabilities, which we implemented according to the following two models:

- Single- and two-qubit gates are characterized by the same arbitrary parameters (p_x, p_z);
- Equal error probabilities in the X and Z directions, but they take generally different values for single-qubit gates ($p_1 = p_x = p_z$) and two-qubit gates ($p_2 = p_x = p_z$).

The time step that determines the best resolution trade-off in view of investigating the DQPT point is $\Delta t = 0.1$. In the averaged trace distance (31), the argument ρ_{ibmq} is averaged over ten experimental realizations of the density matrix evolution, as represented in Figure 7, while ρ_{sim} is averaged over 20 noise realizations for each time step of the evolution. The contour plots in Figure 8 interpolate the evaluation over a grid composed by 31×31 points with spacing 10^{-3}. They describe how distinguishable both aforementioned noise models are with respect to the evolution in `ibmq_manila`. The minimum value for both models in Panels (a)–(b) is obtained by a further evaluation along the elongated direction, and it is approximately equal to 23.5×10^{-2}, corresponding to $(p_x, p_z) \simeq (1.1 \times 10^{-2}, 1.5 \times 10^{-2})$ in the case of Panel (a) and $(p_1, p_2) \simeq (1 \times 10^{-2}, 1.6 \times 10^{-2})$ in the case of Panel (b). These values are used in Figure 9 to compare the evolution of physical states. In Panels (a)–(d), the overall behavior characterized by a convergence towards the maximally mixed state is captured by the noise models, but non-negligible deviations corresponding to the probability $|\langle\psi_e|\psi(t)\rangle|^2$ in Panel (c) are still not captured by the model, probably because they are driven by coherently accumulated errors, not included for stand-alone gates in current noise models' implementation. A comparable high number of single- and two-qubit gates makes the two noise models overlap, as represented in Figure 8, so we can focus on the simpler one described by the probabilities (p_x, p_z). Such a probability array is denoted as **p** in Figure 9e–h, where the comparison of the reduced noise regimes aimed at estimating a threshold such that a revival is observed after the first DQPT. This translates into the research of a non-monotonic behavior of the Loschmidt echo, which requires an overall error probability per gate ten-times lower than in current implementations.

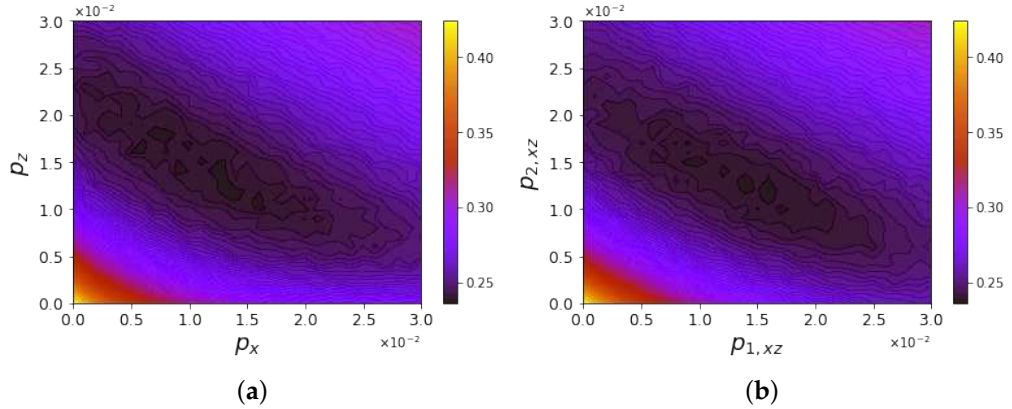

Figure 8. Averaged trace distance $\overline{T(\rho_{\text{ibmq}}, \rho_{\text{sim}})}$ of the evolution yielded in the first three time steps by `ibmq_manila` and the simulated noise models. In Panel (**a**), probability parameters (p_x, p_z) are related to the X and Z errors, while, in Panel (**b**), $(p_{1,xz}, p_{2,xz})$ refer to the error probabilities in the single- and two-qubit gates, respectively, in the case in which Y errors are neglected.

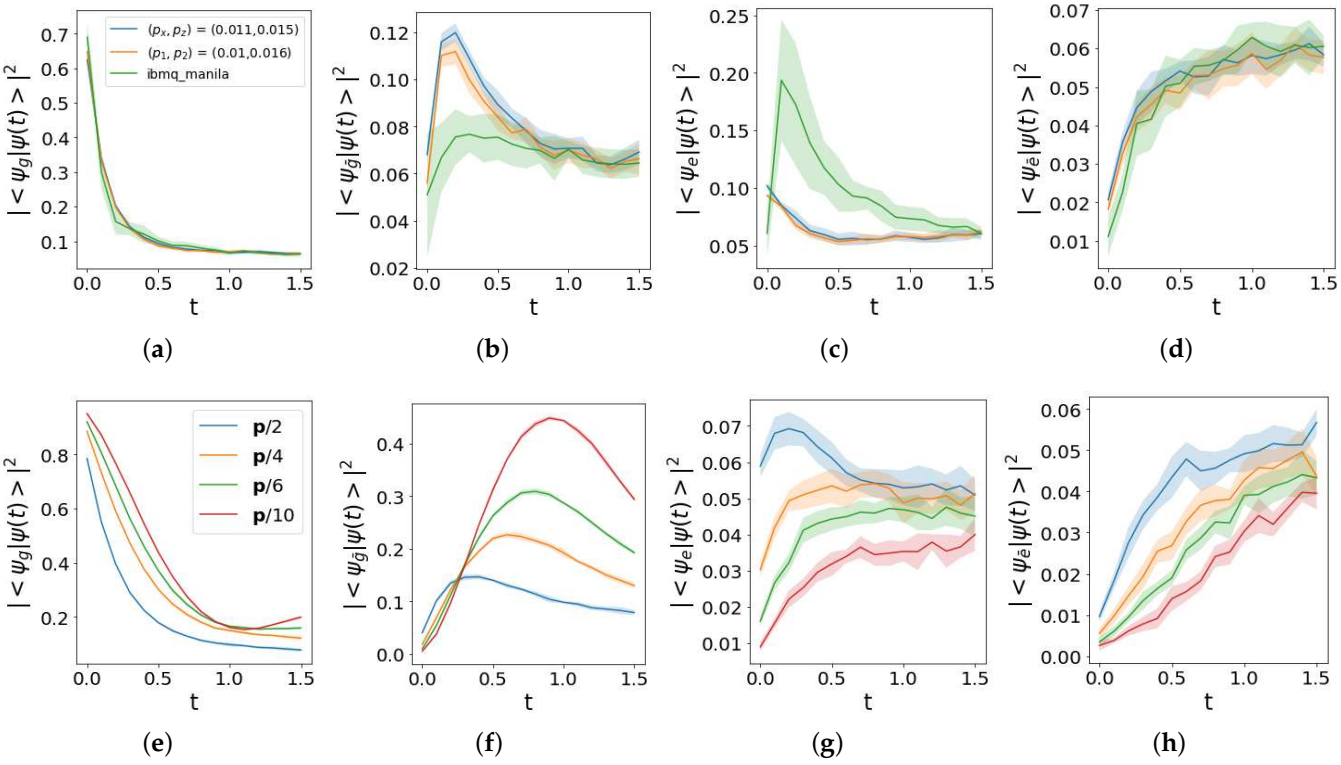

Figure 9. Noise model implemented in the qiskit simulation with Trotter step $\Delta t = 0.1$. In Panels (**a**–**d**), we use the optimal error probabilities determined in Figure 6–8. In Panels (**e**–**h**), such a probability array is denoted by **p** to compare different noise regimes in order to observe a revival following the first dynamical quantum phase transition. In all plots, time is expressed in units of m^{-1}.

4. Discussion

Error correction and mitigation techniques are crucial for NISQ devices in order to efficiently simulate the targeted dynamics [34–36]. An example was given in [37], concerning the real-time dynamics on IBM Quantum of a periodic lattice model for a $1+1$ QED model with $N = 4$ matter sites. There, the discretization of the gauge degrees of freedom was based on a different (non-unitary) truncation. Moreover, the targeted quantities were the vacuum energy and pair production, without a focus on the observation of DQPTs. The exploitation of parity sectors and allowed momenta entails a large reduction of the required qubit number, yielding a scheme able to constrain the evolution in the

physical subspace. The reduced Hamiltonian for the matter degrees of freedom in the targeted sector generates a Trotter dynamics implemented in circuits through the Cartan decomposition. Aiming at the zero noise extrapolation, a procedure adopting repeated application of noisy $CNOT$ gates, was implemented. The circuit depth for each time step increases with respect to the decomposition described in this work, thus allowing us to estimate our targeted first DQPT (with time step $\Delta t = 0.1$) corresponding to the T_2 coherence time, because of the 10-time-step limit mentioned in [37]. Indeed, the total number of circuit moments in our Trotter evolution with 10 steps is equal to 200, as shown in Figure 4. We have to include the ground state preparation depth in Figure 3, because of the $SWAP$ gates related to three $CNOT$ between non-nearest neighbor qubits. The maximal gate temporal extent allowed by the coherence time is slightly lower than the effective one, thus signaling an overestimation of our error probabilities.

The comparison of our results with an ion trap simulation of the lattice Schwinger model with $N = 4$ matter sites in [4] has to take into account the much lower number of Mølmer–Sørensen gates, determined by the higher value of the time step. This is related to the different purpose of the aforementioned work, which aimed at characterizing the pair production mechanism.

The evolution in the proximity of a DQPT is considerably more affected by noise [50,51], as simulated for a transverse field Ising model [40] with error rates comparable to those obtained in our study. Nonetheless, the Hamiltonian terms of an Ising model concern at most spin pairs, thus reducing the circuit complexity for Trotter product formulas. In the case of commuting Hamiltonian terms, at the basis of plaquette dynamics without matter degrees of freedom [38], the Trotter product is not required, thus yielding a further reduction of the circuit depth. Concerning the estimated error probabilities in our analysis, their magnitudes were confirmed in the study of scalar Yukawa coupling [69].

The current experimental realization of ion traps and Rydberg atoms in optical lattices shows a higher value for the average gate fidelity of entangling gates [5,70,71]. The introduction of thermal effects, as well as an increased number of parameters for gates' errors must be considered in order to improve the proposed noise models. Such a detailed description is motivated by the determined "optimal" error probabilities for ground state preparation, which do not coincide with those characterizing time evolution. Moreover, the coherent error accumulation would require more sophisticated noise models, such as correlated dissipation in subsequent quantum channels. The inclusion of error correction and mitigation [37–40] will be investigated in future research to keep the dynamics in the physical subspace and to balance the noise affecting DQPTs' observation.

5. Conclusions

We studied the possibility of simulating the real-time dynamics of a model of QED in $1 + 1$ dimensions, on an elementary lattice composed of two fermionic sites, implemented on IBM Quantum [1]. More specifically, we analyzed the dynamics after a mass quench, close to a dynamical quantum phase transition. The considered quench protocol requires ground state preparation, based on an optimized circuit able to outperform built-in functions, as measured by fidelity with the ideal state. Limitations in observing DQPTs were described in terms of the error probabilities associated with each gate. Different noise models were simulated and compared to capture the main features of the measured evolution, thus determining a marginal contribution of noise along the Y direction. These minimal models revealed the partial observation of the targeted DQPTs' phenomena in circuit implementations with a reduced error probability. The estimated error rate also indicated a promising implementation on ion traps, such as those available in the IonQ platform [72].

Author Contributions: Conceptualization, formal analysis, software, writing—original draft preparation: D.P.; writing—review and editing: L.C., P.F., C.L., S.P. and F.V.P.; supervision and project coordination: P.F. All authors have read and agreed to the published version of the manuscript.

Funding: D.P. is supported by Regione Puglia and by the QuantERA ERA-NET Cofund in Quantum Technologies (Grant No. 731473), the project Quantum Computing Solutions for High-Energy Physics (QuantHEP). We acknowledge financial support from PNRR MUR Projects PE0000023-NQSTI and CN00000013-Italian Research Center on HPC, Big Data and Quantum Computing. P.F. and S.P. are partially supported by Istituto Nazionale di Fisica Nucleare (INFN) through the project "QUANTUM". P.F. is partially supported by the Italian National Group of Mathematical Physics (GNFM-INdAM).

Institutional Review Board Statement: Not applicable.

Informed Consent Statement: Not applicable.

Data Availability Statement: The data presented in this study are available upon request from the corresponding author.

Acknowledgments: We acknowledge the use of IBM Quantum services for this work. The views expressed are those of the authors and do not reflect the official policy or position of IBM nor the IBM Quantum team. Numerical simulations were implemented in ReCaS Bari [73].

Conflicts of Interest: The authors declare no conflict of interest.

Abbreviations

The following abbreviations are used in this manuscript:

NISQ	Noisy intermediate-scale quantum devices
QED	Quantum electrodynamics
DQPT	Dynamical quantum phase transition

Appendix A

The $1+1$ QED Hamiltonian for a periodic lattice with $N=2$ matter sites, analyzed in Section 2.1 and referring to states in the physical subspace $\mathscr{H}_G$ in Figure 1, is

$$\begin{aligned} H(m,J) = {} & m\left(|e^+e^-\rangle_L\langle e^+e^-| + |e^+e^-\rangle_R\langle e^+e^-| - |vac\rangle_-\langle vac| - |vac\rangle_+\langle vac|\right) \\ & + \frac{J}{2}\left(|vac\rangle_{-\,L}\langle e^+e^-| + |vac\rangle_{-\,R}\langle e^+e^-| + |e^+e^-\rangle_{L\,+}\langle vac| + |e^+e^-\rangle_{R\,+}\langle vac| + \text{H.c.}\right), \end{aligned} \tag{A1}$$

in a total Hilbert space with dim $\mathscr{H} = 2^{2N}$. By exploiting parity symmetry [50], the eigenstates of the positive sector read

$$|\psi_{g/\bar{g}}\rangle = a_{g/\bar{g}}(|vac\rangle_+ + |vac\rangle_-) + b_{g/\bar{g}}(|e^+e^-\rangle_L + |e^+e^-\rangle_R) \tag{A2}$$

with the coefficients ratio $p_{g/\bar{g}} = \frac{m\mp\sqrt{m^2+J^2}}{J}$ being obtained by imposing $H|\psi_{g/\bar{g}}\rangle = E_{g/\bar{g}}|\psi_{g/\bar{g}}\rangle$. The amplitudes are equal to $a_{g/\bar{g}} = \left[2\left(1+p_{g/\bar{g}}^2\right)\right]^{-\frac{1}{2}}$ and $b_{g/\bar{g}} = a_{g/\bar{g}}p_{g/\bar{g}}$, thus yielding the Hamiltonian diagonalization with $U = (|\psi_e\rangle, |\psi_{\bar{e}}\rangle, |\psi_g\rangle, |\psi_{\bar{g}}\rangle)^\intercal$:

$$U^\dagger H(m,J)U = \text{diag}\{E_e, E_{\bar{e}}, E_g, E_{\bar{g}}\} = \text{diag}\left\{-m, m, -\sqrt{m^2+J^2}, \sqrt{m^2+J^2}\right\}, \tag{A3}$$

where the negative parity eigenstates are $|\psi_e\rangle = \frac{1}{\sqrt{2}}(|vac\rangle_+ - |vac\rangle_-)$ and $|\psi_{\bar{e}}\rangle = \frac{1}{\sqrt{2}}(|e^+e^-\rangle_L - |e^+e^-\rangle_R)$.The evaluation of the expectation values allows us to identify a destructive interference underlying the suppression of hopping contributions in the negative parity sector.

The quench at $t = 0$ inverts the mass sign $H(m, J) \longrightarrow H(-m, J)$, whose diagonalization with respect to the previous eigenstates yields a Rabi model in the positive parity sector, while giving just an eigenvalue sign inversion in the negative parity sector, namely

$$U^\dagger H(-m,J)U = H^{(-)} \oplus H^{(+)} = \begin{pmatrix} m & 0 & 0 & 0 \\ 0 & -m & 0 & 0 \\ 0 & 0 & -\frac{J^2-m^2}{\sqrt{m^2+J^2}} & \frac{2Jm}{\sqrt{m^2+J^2}} \\ 0 & 0 & \frac{2Jm}{\sqrt{m^2+J^2}} & \frac{J^2-m^2}{\sqrt{m^2+J^2}} \end{pmatrix}, \tag{A4}$$

with the eigenstate coefficients' transformation:

$$\begin{aligned} b_{\bar{g}} &\longrightarrow b'_{\bar{g}} = -b_g, \quad a_{\bar{g}} \longrightarrow a'_{\bar{g}} = a_g, \\ b_g &\longrightarrow b'_g = -b_{\bar{g}}, \quad a_g \longrightarrow a'_g = a_{\bar{g}}. \end{aligned} \tag{A5}$$

Finally, the analytical expression of the Loschmidt amplitude is obtained by exploiting the completeness relation and reads

$$\begin{aligned} \mathcal{G}(t) &= \langle\psi_g|\psi(t)\rangle = \langle\psi_g|\mathrm{e}^{-\mathrm{i}H(-m,J)t}|\psi_g\rangle = (2a_g^2 - 2b_g^2)^2\mathrm{e}^{-\mathrm{i}E_g t} + (2a_g a_{\bar{g}} - 2b_g b_{\bar{g}})^2\mathrm{e}^{-\mathrm{i}E_{\bar{g}} t} = \\ &= (2a_g^2 - 2b_g^2)^2\mathrm{e}^{-\mathrm{i}E_g t}\left(1 + \left(\frac{\widetilde{J}}{\sqrt{1+\widetilde{J}^2}}\left(1 + \frac{\widetilde{J}^2}{1-\sqrt{1+\widetilde{J}^2}}\right)\right)^2 \mathrm{e}^{-\mathrm{i}(E_{\bar{g}}-E_g)t}\right) \\ &= (2a_g^2 - 2b_g^2)^2\mathrm{e}^{-\mathrm{i}E_g t}(1 + \widetilde{J}^2\mathrm{e}^{-\mathrm{i}(E_{\bar{g}}-E_g)t}), \end{aligned} \tag{A6}$$

with a rescaled coupling $\widetilde{J} = J/m$.

Appendix B

The implementation of the noise models occurs through the application of quantum channels. An open quantum system composed by a single qubit is described using a density matrix, with components in the Pauli basis $\{G_k\}_{k=0,1,2,3} = \{\sigma_k/\sqrt{2}\}_{k=0,1,2,3}$:

$$\rho(t) = \sum_{k=0}^{3} r_k(t) G_k, \tag{A7}$$

consisting of its vectorized form. The dynamics is ruled by a master equation:

$$\frac{\mathrm{d}\rho(t)}{\mathrm{d}t} = \Lambda[\rho(t)], \tag{A8}$$

which we represent in a matrix form $L_{k\ell} = \mathrm{Tr}\{G_k \Lambda[G_\ell]\}$, which is time independent in the Markovian case:

$$\frac{\mathrm{d}r_k(t)}{\mathrm{d}t} = \sum_{\ell=0}^{3} L_{k\ell} r_\ell(t). \tag{A9}$$

In the `AerSimulator` noise model, the simulations of single qubits exploit the Kraus–Sudarshan representation, a linear map acting on density matrix states:

$$\rho(t) = \mathcal{D}_t[\rho(0)] = \sum_{i=0}^{3} K_i(t)\rho(0)K_i^\dagger(t), \tag{A10}$$

whose matrix representation $D_{k\ell}(t) = \mathrm{Tr}\{G_k \mathcal{D}_t[G_\ell]\}$ yields

$$r_k(t) = \sum_{\ell=0}^{3} D_{k\ell}(t) r_\ell(0). \tag{A11}$$

The composition of this linear map with the master equation reads $\frac{\mathrm{d}\mathcal{D}_t}{\mathrm{d}t} = \Lambda \circ \mathcal{D}_t$, by the matrix expression:

$$\frac{\mathrm{d}D_{k\ell}(t)}{\mathrm{d}t} = \sum_{m=0}^{3} L_{km} D_{m\ell}(t), \tag{A12}$$

in general consisting of a system of ordinary differential equations, which leads to the semigroup solution $\mathbb{D}(t) = \exp\{t\mathbb{L}\}$, with $\mathbb{D}(0) = \mathbb{1}$ [74].

Depolarizing channels are common examples, defined by an equal probability $p(t)$ for errors along any direction:

$$K_0(t) = \sqrt{1 - p(t)}\,\mathbb{1}, \quad K_i(t) = \sqrt{\frac{p(t)}{3}}\,\sigma_i, \tag{A13}$$

with Markovian master equation:

$$\frac{\mathrm{d}\rho(t)}{\mathrm{d}t} = \Lambda[\rho(t)] = \frac{\gamma}{4}\sum_{k=0}^{3}[\sigma_k \rho(t) \sigma_k - \rho(t)]. \tag{A14}$$

The corresponding Kraus–Sudarshan decomposition and channel matrix form read, respectively,

$$\begin{aligned} D_{k\ell}(t) &= (1 - p(t))\delta_{k\ell} + p(t)\left[2\delta_{k0}\delta_{\ell 0} - \delta_{k\ell} + \frac{2}{3}\sum_i \delta_{ki}\delta_{\ell i}\right], \\ L_{k\ell} &= \frac{3}{4}\gamma\delta_{k\ell} + \frac{3}{4}\gamma\left[2\delta_{k0}\delta_{\ell 0} - \delta_{k\ell} + \frac{2}{3}\sum_i \delta_{ki}\delta_{\ell i}\right], \end{aligned} \tag{A15}$$

composed in order to produce a single ordinary differential equation $\frac{\mathrm{d}\mathbb{D}(t)}{\mathrm{d}t} = \mathbb{L}\mathbb{D}(t)$, whose solution converges towards the maximally mixed state:

$$p(t) = \frac{3}{4}(1 - \mathrm{e}^{-\gamma t}). \tag{A16}$$

The quantum channels presented in Equation (19) generalize the previous case with parameters $p_x(t)$, $p_y(t)$, and $p_z(t)$. The `AerSimulator` implementation does not show any time dependence, adopting a fixed error rate along each direction during gates' application, while its inclusion allows the exploitation of quantum trajectories [75].

The Markovian master equation assigns a specific decoherence rate to each direction:

$$\frac{\mathrm{d}\rho(t)}{\mathrm{d}t} = \Lambda[\rho(t)] = \frac{1}{4}\sum_{k=0}^{3}\gamma_k[\sigma_k \rho(t) \sigma_k - \rho(t)], \tag{A17}$$

leading to the matrix representation of both the Kraus–Sudarshan map and the channel:

$$\begin{aligned} D_{k\ell}(t) &= (1 - p_x(t) - p_y(t) - p_z(t))\delta_{k\ell} + \big[(2\delta_{k0}\delta_{\ell 0} - \delta_{k\ell})(p_x(t) + p_y(t) + p_z(t)) \\ &\quad + 2(p_x(t)\delta_{k1}\delta_{\ell 1} + p_y(t)\delta_{k2}\delta_{\ell 2} + p_z(t)\delta_{k3}\delta_{\ell 3})\big], \\ L_{k\ell} &= \frac{1}{4}(\gamma_x + \gamma_y + \gamma_z)\delta_{k\ell} + \frac{1}{4}\big[(2\delta_{k0}\delta_{\ell 0} - \delta_{k\ell})(\gamma_x + \gamma_y + \gamma_z) \\ &\quad + 2(\gamma_x\delta_{k1}\delta_{\ell 1} + \gamma_y\delta_{k2}\delta_{\ell 2} + \gamma_z\delta_{k3}\delta_{\ell 3})\big], \end{aligned} \tag{A18}$$

or, in a compact form,

$$\begin{aligned} \mathbb{D}(t) &= \mathrm{diag}\{1, 1 - 2(p_y(t) + p_z(t)), 1 - 2(p_x(t) + p_z(t)), 1 - 2(p_x(t) + p_y(t))\}, \\ \mathbb{L} &= \mathrm{diag}\left\{0, -\frac{1}{2}(\gamma_y + \gamma_z), -\frac{1}{2}(\gamma_x + \gamma_z), -\frac{1}{2}(\gamma_x + \gamma_y)\right\}. \end{aligned} \tag{A19}$$

The corresponding system of ordinary differential equation reads

$$\begin{cases} \dot{p}_y(t) + \dot{p}_z(t) = \frac{1}{4}(\gamma_y + \gamma_z)[1 - 2(p_y(t) + p_z(t))], \\ \dot{p}_x(t) + \dot{p}_z(t) = \frac{1}{4}(\gamma_x + \gamma_z)[1 - 2(p_x(t) + p_z(t))], \\ \dot{p}_x(t) + \dot{p}_y(t) = \frac{1}{4}(\gamma_y + \gamma_z)[1 - 2(p_x(t) + p_y(t))], \end{cases} \tag{A20}$$

with explicit time-dependent solutions:

$$\begin{aligned} p_x(t) &= \frac{1}{4}(1 - \mathrm{e}^{-(\gamma_x+\gamma_y)\frac{t}{2}} - \mathrm{e}^{-(\gamma_x+\gamma_z)\frac{t}{2}} + \mathrm{e}^{-(\gamma_y+\gamma_z)\frac{t}{2}}), \\ p_y(t) &= \frac{1}{4}(1 - \mathrm{e}^{-(\gamma_x+\gamma_y)\frac{t}{2}} + \mathrm{e}^{-(\gamma_x+\gamma_z)\frac{t}{2}} - \mathrm{e}^{-(\gamma_y+\gamma_z)\frac{t}{2}}), \\ p_z(t) &= \frac{1}{4}(1 + \mathrm{e}^{-(\gamma_x+\gamma_y)\frac{t}{2}} - \mathrm{e}^{-(\gamma_x+\gamma_z)\frac{t}{2}} - \mathrm{e}^{-(\gamma_y+\gamma_z)\frac{t}{2}}), \end{aligned} \tag{A21}$$

whose sum reduces to Equation (A16) when $\gamma_x = \gamma_y = \gamma_z = \gamma$.

References

1. IBM Quantum. Available online: https://quantum-computing.ibm.com/ (accessed on 28 March 2023).
2. Bardin, J.; Jeffrey, E.; Lucero, E.; Huang, T.; Naaman, O.; Barends, R.; White, T.; Giustina, M.; Sank, D.; Roushan, P.; et al. A 28 nm Bulk-CMOS 4-to-8GHz <2mW Cryogenic Pulse Modulator for Scalable Quantum Computing. In Proceedings of the 2019 International Solid State Circuits Conference, San Francisco, CA, USA, 17–21 February 2019.
3. Garcia-Alonso, J.; Rojo, J.; Valencia, D.; Moguel, E.; Berrocal, J.; Murillo, J.M. Quantum Software as a Service Through a Quantum API Gateway. *IEEE Internet Comput.* **2021**, *26*, 34–41. [CrossRef]
4. Martinez, E.A.; Muschik, C.A.; Schindler, P.; Nigg, D.; Erhard, A.; Heyl, M.; Hauke, P.; Dalmonte, M.; Monz, T.; Zoller, P.; et al. Real-time dynamics of lattice gauge theories with a few-qubit quantum computer. *Nature* **2016**, *534*, 516–519. [CrossRef] [PubMed]
5. Levine, H.; Keesling, A.; Omran, A.; Bernien, H.; Schwartz, S.; Zibrov, A.S.; Endres, M.; Greiner, M.; Vuletic, V.; Lukin, M.D. High-Fidelity Control and Entanglement of Rydberg-Atom Qubits. *Phys. Rev. Lett.* **2018**, *121*, 123603. [CrossRef]
6. Wright, K.; Beck, K.M.; Debnath, S.; Amini, J.M.; Nam, Y.; Grzesiak, N.; Chen, J.-S.; Pisenti, N.C.; Chmielewski, M.; Collins, C.; et al. Benchmarking an 11-qubit quantum computer. *Nat. Comm.* **2019**, *10*, 5464. [CrossRef] [PubMed]
7. Wang, Y.; Crain, S.; Fang, C.; Zhang, B.; Huang, S.; Liang, Q.; Leung, P.H.; Brown, K.R.; Kim, J. High-Fidelity Two-Qubit Gates Using a Microelectromechanical-System-Based Beam Steering System for Individual Qubit Addressing. *Phys. Rev. Lett.* **2020**, *125*, 150505. [CrossRef]
8. Nielsen, E.; Gamble, J.K.; Rudinger, K.; Scholten, T.; Young, K.; Blume-Kohout, R. Gate Set Tomography. *Quantum* **2021**, *5*, 557. [CrossRef]
9. Zhong, H.-S.; Wang, H.; Deng, Y.-H.; Chen, M.-C.; Peng, L.-C.; Luo, Y.-H.; Qin, J.; Wu, D.; Ding, X.; Hu, Y.; et al. Quantum computational advantage using photons. *Science* **2020**, *370*, 6523. [CrossRef]
10. Madsen, L.S.; Laudenbach, F.; Askarani, M.F.; Rortais, F.; Vincent, T.; Bulmer, J.F.F.; Miatto, F.M.; Neuhaus, L.; Helt, L.G.; Collins, M.J.; et al. Quantum computational advantage with a programmable photonic processor. *Nature* **2022**, *606*, 75–81. [CrossRef]
11. Magano, D.; Kumar, A.; Kalis, M.; Locans, A.; Glos, A.; Pratapsi, S.; Quinta, G.; Dimitrijevs, M.; Rivoss, A.; Bargassa, P.; et al. Quantum speedup for track reconstruction in particle accelerators. *Phys. Rev. D* **2022**, *105*, 076012. [CrossRef]
12. Delgado, A.; Hamilton, K.E.; Date, P.; Vlimant, J.; Magano, D.; Omar, Y.; Bargassa, P.; Francis, A.; Gianelle, A.; Sestini, L.; et al. Quantum Computing for Data Analysis in High-Energy Physics. *arXiv* **2022**, arXiv:2203.08805.
13. Bargassa, P.; Cabos, T.; Choi, A.C.O.; Hessel, T.; Cavinato, S. Quantum algorithm for the classification of supersymmetric top quark events. *Phys. Rev. D* **2021**, *104*, 096004. [CrossRef]
14. Pires, D.; Omar, Y.; Seixas, J. Adiabatic Quantum Algorithm for Multijet Clustering in High Energy Physics. *arXiv* **2020**, arXiv:2012.14514.
15. Felser, T.; Trenti, M.; Sestini, L.; Gianelle, A.; Zuliani, D.; Lucchesi, D.; Montangero, S. Quantum-inspired Machine Learning on high-energy physics data. *NPJ Quantum Inf.* **2021**, *7*, 111. [CrossRef]
16. Rothe, H.J. *Lattice Gauge Theories*; World Scientific: Singapore, 1992.
17. Montvay, I.; Münster, G. *Quantum Fields on a Lattice*; Cambridge University Press: Cambridge, UK, 1994.
18. DeGrand, T.; DeTar, C. *Lattice Methods for Quantum Chromodynamics*; World Scientific: Singapore, 2006.
19. Gattringer, C.; Lang, C.B. *Quantum Chromodynamics on the Lattice*; Springe: Berlin/Heidelberg, Germany, 2010.
20. Knechtli, F.; Günther, M.; Peardon, M. *Lattice Quantum Chromodynamics Practice Essentials*; Springer: Berlin/Heidelberg, Germany, 2016.
21. Gattringer, C.; Langfeld, K. Approaches to the sign problem in lattice field theory. *Int. J. Mod. Phys. A* **2016**, *31*, 1643007. [CrossRef]
22. Fukushima, K.; Hatsuda, T. The phase diagram of dense QCD. *Rep. Prog. Phys.* **2011**, *74*, 014001. [CrossRef]

23. Endrődi, G.; Fodor, Z.; Katz, S.D.; Szabó, K.K. The QCD phase diagram at nonzero quark density. *J. High Energy Phys.* **2011**, *2011*, 1–14. [CrossRef]
24. Schollwöck, U. The density-matrix renormalization group. *Rev. Mod. Phys.* **2005**, *77*, 259. [CrossRef]
25. Schollwöck, U. The density-matrix renormalization group in the age of matrix product states. *Ann. Phys.* **2011**, *326*, 96. [CrossRef]
26. Orús, R. A practical introduction to tensor networks: Matrix product states and projected entangled pair states. *Ann. Phys.* **2014**, *349*, 117. [CrossRef]
27. Montangero, S. *Introduction to Tensor Network Methods: Numerical Simulations of Low-Dimensional Many-Body Quantum Systems*; Springer International Publishing: New York, NY, USA, 2018.
28. Sengupta, R.; Adhikary, S.; Oseledets, I.; Biamonte, J. Tensor networks in machine learning. *arXiv* **2022**, arXiv:2207.02851.
29. Magnifico, G.; Felser, T.; Silvi, P.; Montangero, S. Lattice Quantum Electrodynamics in (3+1)-dimensions at finite density with Tensor Networks. *Nat. Commun.* **2021**, *12*, 3600. [CrossRef] [PubMed]
30. Felser, T.; Silvi, P.; Collura, M.; Montangero, S. Two-dimensional quantum-link lattice Quantum Electrodynamics at finite density. *Phys. Rev. X* **2020**, *10*, 041040. [CrossRef]
31. Ercolessi, E.; Facchi, P.; Magnifico, G.; Pascazio, S.; Pepe, F.V. Phase transitions in $\mathbb{Z}_n$ gauge models: Towards quantum simulations of the Schwinger-Weyl QED. *Phys. Rev. D* **2018**, *98*, 074503. [CrossRef]
32. Magnifico, G.; Dalmonte, M.; Facchi, P.; Pascazio, S.; Pepe, F.V.; Ercolessi, E. Real Time Dynamics and Confinement in the $\mathbb{Z}_n$ Schwinger-Weyl lattice model for $1+1$ QED. *Quantum* **2020**, *4*, 281. [CrossRef]
33. Rigobello, M.; Notarnicola, S.; Magnifico, G.; Montangero, S. Entanglement generation in $(1+1)D$ QED scattering processes. *Phys. Rev. D* **2021**, *104*, 114501. [CrossRef]
34. Roffe, J. Quantum error correction: An introductory guide. *Cont. Phys.* **2019**, *60*, 226–245. [CrossRef]
35. Giurgica-Tiron, T.; Hindy, Y.; LaRose, R.; Mari, A.; Zeng, W.J. Digital zero noise extrapolation for quantum error mitigation. In Proceedings of the IEEE International Conference on Quantum Computing and Engineering (QCE), Denver, CO, USA, 12–16 October 2020.
36. Mari, A.; Shammah, N.; Zeng, W.J. Extending quantum probabilistic error cancellation by noise scaling. *Phys. Rev. A* **2021**, *104*, 052607. [CrossRef]
37. Klco, N.; Dumitrescu, E.F.; McCaskey, A.J.; Morris, T.D.; Pooser, R.C.; Sanz, M.; Solano, E.; Lougovski, P.; Savage, M.J. Quantum-classical computation of Schwinger model dynamics using quantum computers. *Phys. Rev. A* **2018**, *98*, 032331. [CrossRef]
38. Huffman, E.; Vera, M.G.; Banerjee, D. Toward the real-time evolution of gauge-invariant $\mathbb{Z}_2$ and $U(1)$ quantum link models on noisy intermediate-scale quantum hardware with error mitigation. *Phys. Rev. D* **2022**, *106*, 094502. [CrossRef]
39. Gustafson, E.; Dreher, P.; Hang, Z.; Meurice, Y. Indexed improvements for real-time Trotter evolution of a $(1+1)$ field theory using NISQ quantum computers. *Quantum Sci. Technol.* **2021**, *6*, 045020 . [CrossRef]
40. Javanmard, Y.; Liaubaite, U.; Osborne, T.J.; Santos, L. Quantum simulation of dynamical phase transitions in noisy quantum devices. *arXiv* **2022**, arXiv:2211.08318.
41. Mueller, N.; Carolan, J.A.; Connelly, A.; Davoudi, Z.; Dumitrescu, E.F.; Yeter-Aydeniz, K. Quantum computation of dynamical quantum phase transitions and entanglement tomography in a lattice gauge theory. *arXiv* **2022**, arXiv:2210.03089.
42. Nguyen, N.H.; Tran, M.C.; Zhu, Y.; Green, A.M.; Alderete, C.H.; Davoudi, Z.; Linke, N.M. Digital Quantum Simulation of the Schwinger Model and Symmetry Protection with Trapped Ions. *Phys. Rev. X* **2022**, *3*, 020324. [CrossRef]
43. Schweizer, C.; Grusdt, F.; Berngruber, M.; Barbiero, L.; Demler, E.; Goldman, N.; Bloch, I.; Aidelsburger, M. Floquet approach to $\mathbb{Z}_2$ lattice gauge theories with ultracold atoms in optical lattices. *Nat. Phys.* **2019**, *15*, 1168–1173. [CrossRef]
44. Aidelsburger, M.; Barbiero, L.; Bermudez, A.; Chanda, T.; Dauphin, A.; González-Cuadra, D.; Grzybowski, P.R.; Hands, S.; Jendrzejewski, F.; Jünemann, J.; et al. Cold atoms meet lattice gauge theory. *Philos. Trans. R. Soc. A* **2021**, *380*, 20210064. [CrossRef]
45. Halimeh, J.C.; Hauke, P. Staircase Prethermalization and Constrained Dynamics in Lattice Gauge Theories. *arXiv* **2020**, arXiv:2004.07248.
46. Halimeh, J.C.; Hauke, P. Origin of staircase prethermalization in lattice gauge theories. *arXiv* **2020**, arXiv:2004.07254.
47. Halimeh, J.C.; Kasper, V.; Hauke, P. Fate of Lattice Gauge Theories Under Decoherence. *arXiv* **2020**, arXiv:2009.07848.
48. Halimeh, J.C.; Hauke, P. Diffusive-to-ballistic crossover of symmetry violation in open many-body systems. *arXiv* **2020**, arXiv:2010.00009.
49. Notarnicola, S.; Ercolessi, E.; Facchi, P.; Marmo, G.; Pascazio, S.; Pepe, F.V. Discrete Abelian gauge theories for quantum simulations of QED. *J. Phys. A Math. Theor.* **2015**, *48*, 30FT01. [CrossRef]
50. Pedersen, S.P.; Zinner, N.T. Lattice gauge theory and dynamical quantum phase transitions using noisy intermediate-scale quantum devices. *Phys. Rev. B* **2021**, *103*, 235103. [CrossRef]
51. Jensen, R.B.; Pedersen, S.P.; Zinner, N.T. Dynamical quantum phase transitions in a noisy lattice gauge theory. *Phys. Rev. B* **2022**, *105*, 224309. [CrossRef]
52. Shaw, A.F.; Lougovski, P.; Stryker, J.R.; Wiebe, N. Quantum Algorithms for Simulating the Lattice Schwinger Model. *Quantum* **2020**, *4*, 306. [CrossRef]
53. Notarnicola, S.; Collura, M.; Montangero, S. Real-time-dynamics quantum simulation of $(1+1)$-dimensional lattice QED with Rydberg atoms. *Phys. Rev. Res.* **2020**, *2*, 013288. [CrossRef]
54. Mathis, S.V.; Mazzola, G.; Tavernelli, I. Toward scalable simulations of lattice gauge theories on quantum computers. *Phys. Rev. D* **2020**, *102*, 094501. [CrossRef]

55. Dempsey, R.; Klebanov, I.R.; Pufu, S.S.; Zan, B. Discrete chiral symmetry and mass shift in the lattice Hamiltonian approach to the Schwinger model. *Phys. Rev. Res.* **2022**, *4*, 043133. [CrossRef]
56. Zache, T.V.; Mueller, N.; Schneider, J.T.; Jendrzejewski, F.; Berges, J.; Hauke, P. Dynamical Topological Transitions in the Massive Schwinger Model with a θ Term. *Phys. Rev. Lett.* **2019**, *122*, 050403. [CrossRef] [PubMed]
57. Heyl, M. Dynamical quantum phase transitions: A review. *Rep. Prog. Phys.* **2018**, *81*, 054001. [CrossRef] [PubMed]
58. Damme, M.V.; Zache, T.V.; Banerjee, D.; Hauke, P.; Halimeh, J.C. Dynamical quantum phase transitions in spin-S $U(1)$ quantum link models. *Phys. Rev. B* **2022**, *106*, 245110. [CrossRef]
59. Damme, M.V.; Desaules, J.-Y.; Papić, Z.; Halimeh, J.C. The Anatomy of Dynamical Quantum Phase Transitions. *arXiv* **2022**, arXiv:2210.02453.
60. Chandrasekharan, S.; Wiese, U.-J. Quantum link models: A discrete approach to gauge theories. *Nucl. Phys. B* **1997**, *492*, 455. [CrossRef]
61. Kogut, J.; Susskind, L. Hamiltonian formulation of Wilson's lattice gauge theories. *Phys. Rev. D* **1975**, *11*, 2. [CrossRef]
62. Georgopoulos, K.; Emary, C.; Zuliani, P. Modeling and simulating the noisy behavior of near-term quantum computers. *Phys. Rev. A* **2021**, *104*, 062432. [CrossRef]
63. Lamm, H.; Lawrence, S. Simulation of Nonequilibrium Dynamics on a Quantum Computer. *Phys. Rev. Lett.* **2018**, *121*, 170501. [CrossRef]
64. Khaneja, N.; Glaser, S.J. Cartan decomposition of SU(2n) and control of spin systems. *Chem. Phys.* **2001**, *267*, 1–3 . [CrossRef]
65. Khaneja, N.; Brockett, R.; Glaser, S.J. Time optimal control in spin systems. *Phys. Rev. A* **2001**, *63*, 032308. [CrossRef]
66. Vatan, F.; Williams, C. Optimal quantum circuits for general two-qubit gates. *Phys. Rev. A* **2004**, 69, 032315. [CrossRef]
67. Smolin, J.; Gambetta, J.M.; Smith, G. Efficient Method for Computing the Maximum-Likelihood Quantum State from Measurements with Additive Gaussian Noise. *Phys. Rev. Lett.* **2012**, *108*, 070502. [CrossRef]
68. Kardashin, A.S.; Vlasova, A.V.; Pervishko, A.A.; Yudin, D.; Biamonte, J.D. Quantum-machine-learning channel discrimination. *Phys. Rev. A***2022**, *106*, 032409. [CrossRef]
69. Kaldenbach, T.N.; Heller, M.; Alber, G.; Stojanović, V.M. Digital quantum simulation of scalar Yukawa coupling: Dynamics following an interaction quench on IBM Q. *arXiv* **2022**, arXiv:2211.02684.
70. Surace, F.M.; Mazza, P.P.; Giudici, G.; Lerose, A.; Gambassi, A.; Dalmonte, M. Lattice Gauge Theories and String Dynamics in Rydberg Atom Quantum Simulators. *Phys. Rev. X* **2020**, *10*, 021041. [CrossRef]
71. Amitrano, V.; Roggero, A.; Luchi, P.; Turro, F.; Vespucci, L.; Pederiva, F. Trapped-Ion Quantum Simulation of Collective Neutrino Oscillations. *Phys. Rev. D* **2023**, *107*, 023007. [CrossRef]
72. IonQ. Available online: https://ionq.com/ (accessed on 28 March 2023).
73. ReCaS Bari. Available online: https://www.recas-bari.it/index.php/en/ (accessed on 28 March 2023).
74. Andersson, E.; Cresser, J.D.; Hall, M.J.W. Finding the Kraus decomposition from a master equation and vice versa. *J. Mod. Opt.* **2007**, *54*, 12. [CrossRef]
75. Bartolomeo, G.D.; Vischi, M.; Cesa, F.; Wixinger, R.; Grossi, M.; Donadi, S.; Bassi, A. A novel approach to noisy gates for simulating quantum computers. *arXiv* **2023**, arXiv:2301.04173.

Disclaimer/Publisher's Note: The statements, opinions and data contained in all publications are solely those of the individual author(s) and contributor(s) and not of MDPI and/or the editor(s). MDPI and/or the editor(s) disclaim responsibility for any injury to people or property resulting from any ideas, methods, instructions or products referred to in the content.